High-Power Capacitive Power Transfer System With Integrated Multichannel Coupler

Gang Yang, Pan Sun, Enguo Rong, *Member, IEEE*, Xiaochen Zhang, Xusheng Wu, Qijun Deng, and Siqi Li, *Senior Member, IEEE*

***Abstract*—The demand for high-power wireless power transfer systems has been gradually increasing in recent years. In this article, a high-power capacitive power transfer (CPT) system with an integrated multichannel coupler (IMCC) is proposed, which first realizes an output power of more than 10 kW, and the IMCC offers the advantages of reduced compensation inductors, reduced cross-coupling effects, and extendable performance. Since there is a cross-coupling between every two plates, the IMCC results in a circuit model of $15n + 16C_n^2$ coupling capacitors (*n* represents the number of channels). The induced current source model and induced voltage source model are used to model the IMCC, and the effects of cross-coupling mutual capacitances on the system are analyzed. Compared to the four-plate multichannel coupler, the IMCC can reduce the cross-coupling effects in both aligned and misaligned cases. An M-M compensated three-channel CPT prototype with the IMCC is built, achieving an impressive output power of 10.35-kW and dc–dc efficiency of 94.2% with a 50-mm airgap. Experimental results show that the proposed CPT system with the IMCC is suitable for high-power applications and can effectively minimize the cross-coupling effects.**

***Index Terms*—Cross-coupling, high-power capacitive power transfer (CPT), integrated multichannel coupler.**

NOMENCLATURE

T_{i1}–T_{i4}	Primary-side MOSFETs of channel *i*.
D_{i1}–D_{i4}	Secondary-side rectifier diodes of channel *i*.
$V_{\rm DC}$	Total dc input voltage.
I_{in}	Total dc input current.
V_o	Total dc output voltage.
I_o	Total dc output current.
V_{ini}	DC input voltage of channel *i*.
I_{ini}	DC input current of channel *i*.
V_{oi}	DC output voltage of channel *i*.
I_{oi}	DC output current channel *i*.
U_{ini}	Inverter output voltage of channel *i*.
U_{oi}	Rectifier input voltage of channel *i*.
R_L	Load resistance.
$\rm P_{i1}$–$\rm P_{i4}$	Transmission plates of channel *i*.
$\rm P_U, P_L$	Shielding plates.
C_{xy}^i	Coupling capacitors between transmission plates of channel *i*.
$C_{xU,}^{is} C_{xL}^{is}$	Coupling capacitors between transmission plates of channel *i* and shielding plates.
C_{xy}^{ik}	Coupling capacitors between transmission plates of channel *i* and channel *k*.
$C_{i1,} C_{i2}$	Primary and secondary side self-capacitances of channel *i* in ICS model.
$C_{ia,} C_{ib}$	Self-capacitances of port *a* and port *b* of channel *i* in ICS model.
C_{Miakb}	Mutual capacitances between port *a* of channel *i* and port *b* of channel *k* in ICS model.
C_{Mia0s}	Mutual capacitances between port *a* of channel *i* and port *s* of channel 0 (shielding plates) in ICS model.
$C_{Vi1,} C_{Vi2}$	Primary and secondary side self-capacitances of channel *i* in IVS model.
C_{VMi}	Mutual capacitances of channel *i* in IVS model.
C_{Mab}^{ik}	Mutual capacitances between port *a* of channel *i* and port *b* of channel *k* in IVS model.
$X_{CVM\alpha}$	Impedance of the same-side cross-coupling mutual capacitance.
$X_{CVM\beta}$	Impedance of the different-side cross-coupling mutual capacitance.

Received 5 May 2025; revised 8 August 2025; accepted 30 September 2025. Date of publication 3 October 2025; date of current version 23 December 2025. This work was supported in part by the National Natural Science Foundation of China under Grant U24A20144 and in part by the National Key Research and Development Program of China under Grant 2022YFC3102800. Recommended for publication by Associate Editor K.-B. Park. *(Corresponding authors: Enguo Rong; Pan Sun.)*

Gang Yang, Pan Sun, Xiaochen Zhang, and Xusheng Wu are with the School of Electrical Engineering, Naval University of Engineering, Wuhan 430033, China (e-mail: 1507111049@nue.edu.cn; 1007101026@nue.edu.cn; d22380802@nue.edu.cn; 0910061003@nue.edu.cn).

Enguo Rong and Siqi Li are with the Department of Electrical Engineering, Kunming University of Science and Technology, Kunming 650500, China (e-mail: rong@kust.edu.cn; lisiqi@kust.edu.cn).

Qijun Deng is with the Hubei Key Laboratory of Power Equipment & System Security for Integrated Energy, School of Electrical Engineering and Automation, Wuhan University, Wuhan 430072, China (e-mail: dqj@whu.edu.cn).

Color versions of one or more figures in this article are available at https://doi.org/10.1109/TPEL.2025.3617898.

Digital Object Identifier 10.1109/TPEL.2025.3617898

I. INTRODUCTION

WITH the application of wireless power transfer (WPT) technology in electric vehicles [1], [2], electric ships [3], and underwater vehicles [4], [5], research on high-power and high-efficiency WPT systems is becoming more and more popular. Compared to an inductive power transfer (IPT) system, the capacitive power transfer (CPT) system is widely used due to its advantages, such as simple structure, lightweight, and low cost [6], [7], [8], [9]. A 2.4-kW CPT system is designed with an airgap of 150 mm and dc–dc efficiency of 90.8%, demonstrating

the capabilities for kW-class power transfer with a distance around 100 mm and efficiency exceeding 90% [10].

Through years of development, the transmission capability of CPT systems has increased dramatically. In [11], a 6.06-kW CPT system with 60-mm airgap and 92.3% dc–dc efficiency is built, which is the maximum transmission power ever realized. In [12], a 5-kW CPT system with a 100-mm airgap is constructed, achieving a dc–dc efficiency of 96.5%, which stands for the maximum dc–dc efficiency. However, the demand for high-power CPT systems has been increasing for various applications. Taking the railway transportation as an example, the wireless power requirements have exceeded 10 kW [13].

To obtain high-power output with the existing low-power and low-cost semiconductors, multiphase inverters, parallel multi-inverters, multitransmitters, and multichannel topologies are used in WPT systems. For a multiphase inverter topology, the number of bridge arms is not easy to adjust flexibly according to the power due to the fixed structure, which is not suitable for extendable applications [14], [15]. Parallel multi-inverter topology solves the problem of extending, but the loop currents caused by coupling at the output ac side will affect the system performance [16], [17]. Multitransmitter topology utilizes multiple transmitters to simultaneously transmit energy to the receiver to achieve superposition of power, but the single-receiver structure still has limitations of voltage-ampere stress [18], [19]. For a multichannel topology, the transmitted power is increased due to the increased number of transmission paths. It solves the problem of circulating currents due to the connection at the dc side, and the high-voltage and high-power transmission capability can be realized at both the input and output sides. In addition, multichannel topology reduces single-channel capacity requirements, simplifies design, and facilitates modularization to reduce system costs [20], [21], [22]. However, up to now, most of the research works have been focused on IPT systems.

To fulfill the research gap, a dual-input dual-output CPT system with a four-plate dual-channel coupler is proposed for various-power applications [23]. Due to the small self-capacitance value, extra shunt capacitors are connected with the four-plate coupler to increase the self-capacitance and decrease the resonant inductors [10]. However, CPT systems usually have very high voltage stresses among coupler plates, especially for high-power output applications [24]. High voltages across shunt capacitors make them expensive and hard to select. Six-plate coupler is designed to solve this issue and achieve high-power output [11], [25], [26].

In addition, there is cross-coupling between different plates for the multichannel coupler, which is demonstrated to affect the zero phase angle (ZPA) and cause output imbalance between channels [27], [28], [29], [30]. Existing studies show that the cross-coupling in a multichannel coupler can be eliminated by forcing the voltages at the same-side coupling plates in each channel to be equal in modulus but opposite in phase [31], but the symmetrical condition is not easy to realize. Shared inductors are used to achieve same-side decoupling [23], whereas extra elements increase the complexity of the system and affect the extendable performance.

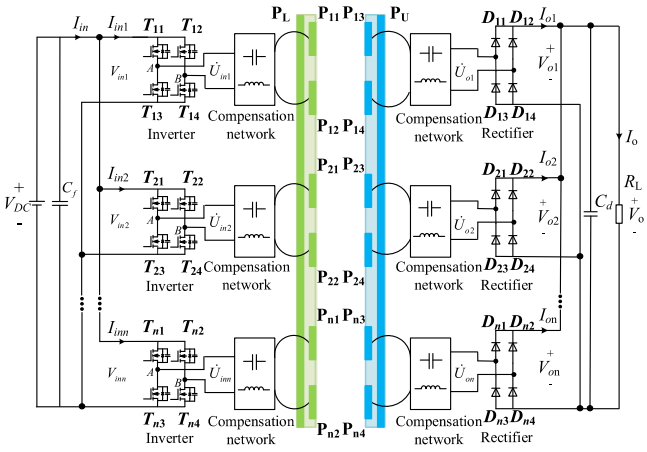

Fig. 1. Topology of proposed multichannel CPT system with the IMCC.

As mentioned above, to achieve high-power output, a CPT system with a multichannel topology is a possible way, and the cross-coupling issues need to be solved. Hence, a CPT system with the integrated multichannel coupler (IMCC) is proposed in this article. The main contributions of this article can be summarized as follows.

1) An integrated multichannel coupler is designed with the advantages of reduced compensation inductors, reduced cross-coupling effects, and extendable performance. A 10.35-kW CPT system with 94.2% dc–dc efficiency is achieved based on the IMCC.
2) The general equivalent circuit model of the IMCC is developed with the induced current source (ICS) model and the induced voltage source (IVS) model. The CPT system with the IMCC is clarified as outer channels and inner channels based on quantitative analysis of cross-coupling mutual capacitances. Further, the cross-coupling effects on an M-M compensated CPT system are analyzed in detail.
3) The capability of reducing cross-coupling effects for the IMCC is analyzed compared with the four-plate multichannel coupler (FMCC) under well-aligned and misaligned conditions.

The remainder of this article is organized as follows: Section II describes the topology of the proposed CPT system and the structure of the IMCC, a general model of the IMCC considering cross-coupling, is developed. In Section III, the influence on the system caused by cross-coupling mutual capacitances is analyzed. Then, the comparison of reducing cross-coupling effects between the IMCC and the FMCC is conducted. An M-M compensated three-channel CPT prototype with the IMCC is built to validate the theoretical analysis in Section IV. Finally, conclusions are summarized in Section V.

II. Modeling of the IMCC

A. Topology of the Proposed CPT System With the IMCC

The topology of the proposed CPT system with the IMCC is shown in Fig. 1, which consists of n single-channel CPT systems. The inverters of each channel are connected in parallel at the dc

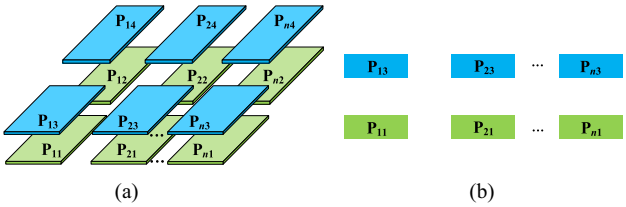

Fig. 2. Structure of the FMCC. (a) Trimetric view. (b) Front view.

input side, and the rectifiers are connected in parallel at the dc output side.

The working principle of the system is as follows: an input dc voltage source V_{DC} is supplied to each channel through the voltage regulator capacitor C_f, and the high-frequency ac voltage $\boldsymbol{U}_{ini}$ is generated by a high-frequency inverter, which is transmitted to the secondary side through the primary compensation network and the coupler. On the secondary side, the high-frequency ac voltage is transmitted through a compensation network, an uncontrolled rectifier, and the filtering capacitor C_d, which finally provides a stable dc voltage to the load R_L. I_{in} represents total dc input current, V_{ini} and I_{ini} represent dc input voltage and current of channel i. I_{oi} represents the dc output current of channel i. V_o and I_o represent load voltage and current. Due to the connection relationship of the primary side in parallel and the secondary side in parallel. The relationships of input and output dc voltage and dc current between channels can be expressed as follows:

$$\begin{cases} V_{\mathrm{DC}} = V_{in1} = V_{in2} = \cdots = V_{ini} = \cdots = V_{inn} \\ I_{in} = \sum_{i=1}^{n} I_{ini} \\ V_o = V_{o1} = V_{o2} = \cdots = V_{oi} = \cdots = V_{on} \\ I_o = \sum_{i=1}^{n} I_{oi} \end{cases}. \tag{1}$$

Under ideal conditions, assuming that the parameters of each channel are consistent, the inputs and outputs of each channel are automatically equalized. The output power of the system can be calculated as follows:

$$P_{\mathrm{out}} = \sum_{i=1}^{n} V_{oi} I_{oi} = n V_{oi} I_{oi} = n P_{oi}. \tag{2}$$

It can be seen from (2) that the output power of the multi-channel system is n times greater than that of the single-channel system under the condition of the same input source.

Fig. 2 shows the structure of the FMCC, which is composed of n pairs of transmitting plates and n pairs of receiving plates.

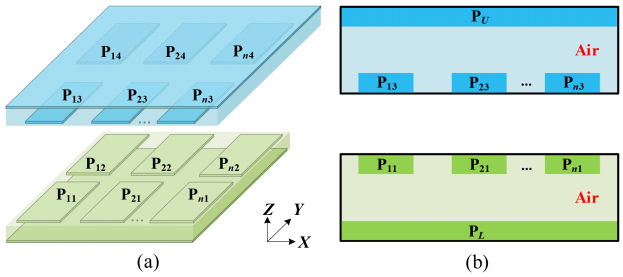

Fig. 3. Structure of the IMCC. (a) Trimetric view. (b) Front view.

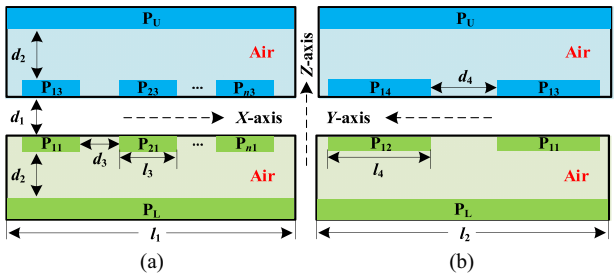

Fig. 4. Size of the IMCC. (a) Front view. (b) Left view.

Compared to the FMCC, the IMCC consists of transmission plates (P_{i1} and P_{i2} are for transmitting side, P_{i3} and P_{i4} are for receiving side) and shielding plates (P_U and P_L represent the upper and the lower shielding plates). Plates P_L and all the transmitting plates are integrated together in a protective box, as well as the plates P_U and all the receiving plates, as shown in Fig. 3. The influence of the protective box on the couplings can be neglected as the thickness is small. All of the transmitting, receiving, and shielding plates are rectangular aluminum plates, the thickness of which is t. The sizes of transmitting and receiving plates are $l_3 \times l_4$, and the size of shielding plates is $l_1 \times l_2$, where l_1, l_3 and l_2, l_4 are the length and width. d_1 is the transmission distance, d_2 is the shielding distance between transmission plates and shielding plates, d_3 is the separation distance between adjacent channels, and d_4 is the separation distance between transmitting/receiving plates, as shown in Fig. 4.

B. Full-Capacitor Model of the IMCC Considering Cross-Coupling

According to the generation mechanism of a capacitor, coupling capacitors exist between any two plates in the IMCC. Define the coupling capacitors between transmission plates in

$$\begin{bmatrix} I_{11} \\ I_{12} \\ I_{21} \\ I_{22} \\ \vdots \\ I_{n1} \\ I_{n2} \\ I_3 \end{bmatrix} = j\omega \begin{bmatrix} C_{11} & -C_{M1112} & -C_{M1121} & -C_{M1122} & \cdots & -C_{M11n1} & -C_{M11n2} & -C_{M110s} \\ -C_{M1211} & C_{12} & -C_{M1221} & -C_{M1222} & \cdots & -C_{M12n1} & -C_{M12n2} & -C_{M120s} \\ -C_{M2111} & -C_{M2112} & C_{21} & -C_{M2122} & \cdots & -C_{M21n1} & -C_{M21n2} & -C_{M210s} \\ -C_{M2211} & -C_{M2212} & -C_{M2221} & C_{22} & \cdots & -C_{M22n1} & -C_{M22n2} & -C_{M220s} \\ \vdots & \vdots & \vdots & \vdots & \ddots & \vdots & \vdots & \vdots \\ -C_{Mn111} & -C_{Mn112} & -C_{Mn121} & -C_{Mn122} & \cdots & C_{n1} & -C_{Mn1n2} & -C_{Mn10s} \\ -C_{Mn211} & -C_{Mn212} & -C_{Mn221} & -C_{Mn222} & \cdots & -C_{Mn2n1} & C_{n2} & -C_{Mn20s} \\ -C_{M0s11} & -C_{M0s12} & -C_{M0s21} & -C_{M0s22} & \cdots & -C_{M0sn1} & -C_{M0sn2} & C_3 \end{bmatrix} \begin{bmatrix} V_{11} \\ V_{12} \\ V_{21} \\ V_{22} \\ \vdots \\ V_{n1} \\ V_{n2} \\ V_3 \end{bmatrix}. \tag{3}$$

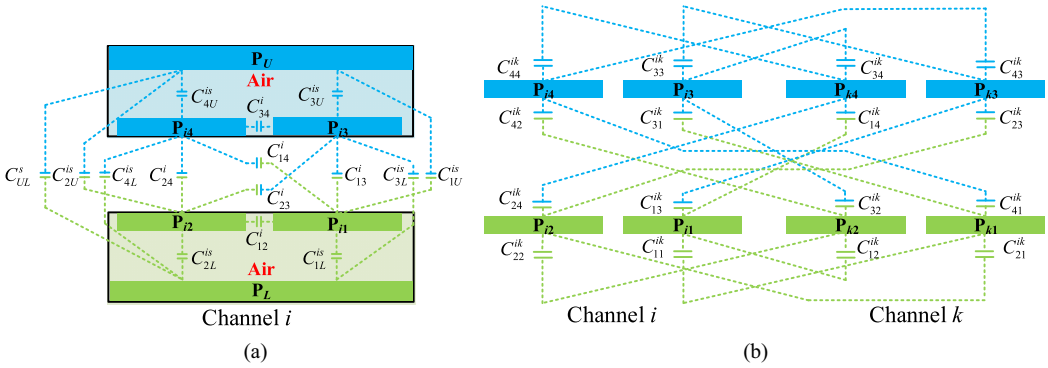

Fig. 5. Coupling capacitors between plates. (a) Coupling capacitors in channel *i*. (b) Cross-coupling capacitors between channel *i* and channel *k*.

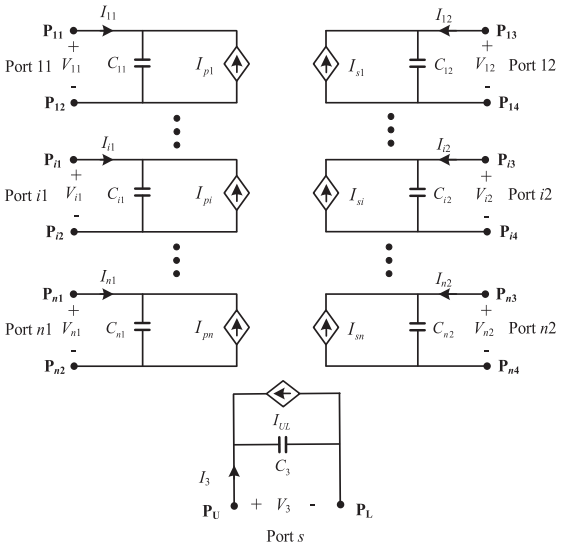

Fig. 6. ICS model of the IMCC.

channel i as $C^{i}{}_{xy}$, where i denotes the channel serial number ($i = 12, \ldots, n$), x and y denote the plate serial number ($x, y = 1, 2, 3, 4$). Define the coupling capacitors between transmission plates of channel i and shielding plates as $C^{is}{}_{xU}$ and $C^{is}{}_{xL}$, and the coupling capacitors between upper and lower shielding plates as $C^{s}{}_{UL}$, as shown in Fig. 5(a). In addition, there are also cross-coupling capacitors between transmission plates of different channels, which are defined as $C^{ik}{}_{xy}$. It devotes the coupling capacitors between plate x of channel i and plate y of channel k, as shown in Fig. 5(b), and it is clearly that $C^{ii}{}_{xy}$ is equal to $C^{i}{}_{xy}$. It can be seen from Fig. 5 that there are $15n + 16C_n^2$ coupling capacitors in the IMCC due to the cross-coupling between channels, which makes modeling of the coupler very complex.

C. ICS Model of the IMCC Considering Cross-Coupling

The widely used ICS model is adopted to represent the equivalent circuit of the IMCC, as shown in Fig. 6. Plates P_{i1} and P_{i2} are connected to the transmitting side circuit and form the port $i1$, plates P_{i3} and P_{i4} are connected to the receiving side circuit and form the port $i2$ ($i = 1, 2, \ldots, n$). Plates P_U and P_L form the port s. Terminal voltages and currents of ports are defined as V_{i1}, I_{i1}, V_{i2}, I_{i2}, V_3, and I_3. C_{i1}, C_{i2}, and C_3 are the self-capacitances of port $i1$, $i2$, and s. C_{Miakb} indicates the cross-coupling mutual capacitances between port a of channel i and port b of channel k. To demonstrate the simplification process, P_U and P_L are defined to form port s of channel 0. C_{Mia0s} represents the mutual capacitances between port a of channel i and port s of channel 0 ($a = 1, 2$, $b = 1, 2$).

The relationships between variables are expressed as (3). The voltage-controlled current sources of each port are defined as I_{pi}, I_{si}, and I_{UL}, which can be calculated as (4).

$$\begin{cases} I_{pi} = j\omega C_{Mi1s} V_3 + j\omega C_{Mi1i2} V_{i2} \\ \qquad +j\omega \sum_{k=1}^{n} \sum_{a=1}^{2} C_{Mi1ka} V_{ka}, \qquad k \neq i \\ I_{si} = j\omega C_{Mi2s} V_3 + j\omega C_{Mi2i1} V_{i1} \\ \qquad +j\omega \sum_{k=1}^{n} \sum_{a=1}^{2} C_{Mi2ka} V_{ka}, \qquad k \neq i \\ I_{UL} = j\omega \sum_{k=1}^{n} \sum_{a=1}^{2} C_{Mska} V_{ka} \end{cases}. \tag{4}$$

In (3) and (4), $\omega = 2\pi f$, where f is the switching frequency.

According to energy arguments, it can be achieved that $C_{Miakb} = C_{Mkbia}$ and $C_{Mia0s} = C_{M0sia}$. To calculate the self-capacitances and cross-coupling mutual capacitances of any two ports, the relationships between the full-capacitor model and the ICS model need to be determined. Take C_{i1} as an example, it can be calculated as follows:

$$C_{i1} = \left. \frac{I_{i1}}{j\omega V_{i1}} \right|_{V_{i1} \neq 0, \quad V_3 = V_{11} = \cdots = V_{n2} = 0}. \tag{5}$$

Fig. 7 shows the simplification process of the full-capacitor model of the IMCC. According to (5), since the voltage of every port is zero except for port $i1$, P_{i3} and P_{i4} of channel i, P_{k1} and P_{k2}, P_{k3} and P_{k4} of channel k, and P_U and P_L are all short-circuited.

Fig. 7(a) shows the full-capacitor model between any two channels (channel i and channel k) in the IMCC, when P_{i3} and

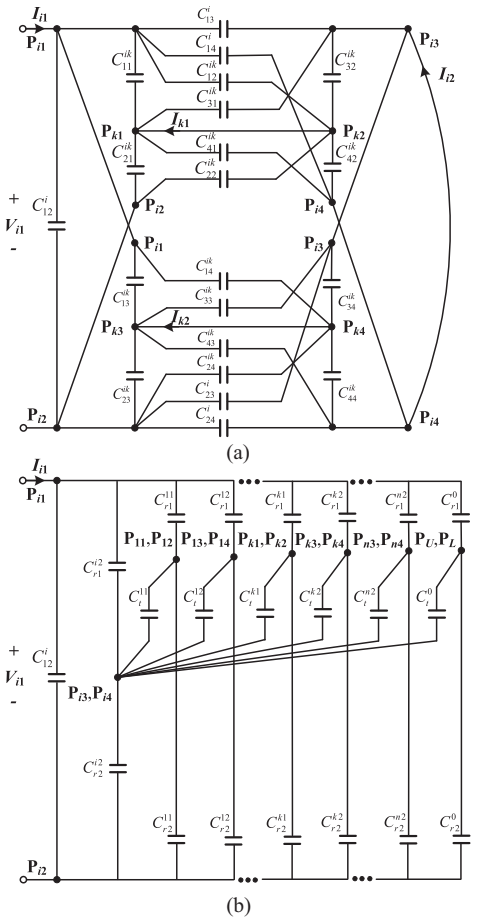

Fig. 7. Simplification of the capacitor model. (a) Full-capacitor model of the IMCC. (b) Combine parallel capacitors.

P_{i4}, P_{k1} and P_{k2}, and P_{k3} and P_{k4} are short-circuited. Full-capacitor model can be simplified to Fig. 7(b) by combining all the parallel capacitors shown as follows:

$$\begin{cases} C_{r1}^{i2} = C_{13}^{i} + C_{14}^{i}; C_{r2}^{i2} = C_{23}^{i} + C_{24}^{i} \\ C_{r1}^{k1} = C_{11}^{ik} + C_{12}^{ik}; C_{r2}^{k1} = C_{21}^{ik} + C_{22}^{ik} \\ C_{t}^{k1} = C_{31}^{ik} + C_{32}^{ik} + C_{41}^{ik} + C_{42}^{ik} \\ C_{r1}^{k2} = C_{13}^{ik} + C_{14}^{ik}; C_{r2}^{k2} = C_{23}^{ik} + C_{24}^{ik} \\ C_{t}^{k2} = C_{33}^{ik} + C_{34}^{ik} + C_{43}^{ik} + C_{44}^{ik} \end{cases}. \tag{6}$$

When $k = 0$, the combined capacitors related to P_U and P_L are as follows:

$$\begin{cases} C_{r1}^{0} = C_{1U}^{is} + C_{1L}^{is}; C_{r2}^{0} = C_{2U}^{is} + C_{2L}^{is} \\ C_{t}^{0} = C_{3U}^{is} + C_{3L}^{is} + C_{4U}^{is} + C_{4L}^{is} \end{cases}. \tag{7}$$

Define V_{Pi1}, V_{Pi2}, V_{Pi3}, and V_{Pi4} as the nodal voltages of P_{i1}, P_{i2}, P_{i3}, and P_{i4}, V_{Pk1} as the nodal voltages of P_{k1} and P_{k2}, V_{Pk2} as the nodal voltages of P_{k3} and P_{k4}, and V_{P0} as the nodal voltages of P_U and P_L. P_{i2} is set as the reference node, the voltage of which is zero. According to Kirchhoff's current law, the equations of nodes in Fig. 7(b) can be expressed as follows:

$$\begin{cases} \left(C_{12}^{i} + C_{r1}^{i2} + \sum_{k=0}^{n} C_{r1}^{ka}\right) V_{Pi1} - C_{r1}^{i2} V_{Pi3} \\ \quad - \sum_{k=0}^{n} C_{r1}^{ka} V_{Pka} = I_{i1}/j\omega \\ C_{12}^{i} V_{Pi1} + C_{r2}^{i2} V_{Pi3} + \sum_{k=0}^{n} C_{r2}^{ka} V_{Pka} = I_{i1}/j\omega \\ \left(C_{r1}^{i2} + C_{r2}^{i2} + \sum_{k=0}^{n} C_{t}^{ka}\right) V_{Pi3} - C_{r1}^{i2} V_{Pi1} - \sum_{k=0}^{n} C_{t}^{ka} V_{Pka} = 0 \\ \sum_{k=0}^{n} \left(C_{r1}^{ka} + C_{r2}^{ka} + C_{t}^{ka}\right) V_{Pka} - V_{Pi1} \sum_{k=0}^{n} C_{r1}^{ka} \\ \quad - V_{Pi3} \sum_{k=0}^{n} C_{t}^{ka} = 0 \end{cases}. \tag{8}$$

It is important to note that the fourth equation in (8) is a summation of the voltage equations of P_{k1}, P_{k2}, P_{k3}, P_{k4}, P_U, and P_L. In (6) and (8), $k = 0, 1, 2, \ldots, n$ and $k \neq i$. The nodal voltages can be calculated as

$$V_{Pka} = \frac{C_{r1}^{ka} V_{Pi1} + C_{t}^{ka} V_{Pi3}}{\left(C_{r1}^{ka} + C_{r2}^{ka} + C_{t}^{ka}\right)}. \tag{9}$$

Substitute (9) into the third equation in (8), V_{Pi3} can be calculated as:

$$V_{Pi3} = \frac{\left[C_{r1}^{i2} + \sum_{k=0}^{n} \frac{C_{t}^{ka} C_{r1}^{ka}}{\left(C_{r1}^{ka} + C_{r2}^{ka} + C_{t}^{ka}\right)}\right]}{\left(C_{r1}^{i2} + C_{r2}^{i2}\right) + \sum_{k=0}^{n} \frac{C_{t}^{ka}\left(C_{r1}^{ka} + C_{r2}^{ka}\right)}{\left(C_{r1}^{ka} + C_{r2}^{ka} + C_{t}^{ka}\right)}} V_{Pi1}. \tag{10}$$

Combining (8), (9), and (10), the self-capacitance C_{i1} is further determined to be (11) shown at the bottom of the next page. When the IMCC is well aligned, the transmitting and receiving plates are symmetric. This means $C^{i}{}_{13} = C^{i}{}_{24}$, $C^{i}{}_{14} = C^{i}{}_{23}$, $C^{ik}{}_{11} = C^{ik}{}_{22}$, $C^{ik}{}_{12} = C^{ik}{}_{21}$, $C^{ik}{}_{13} = C^{ik}{}_{24}$, and $C^{ik}{}_{14} = C^{ik}{}_{23}$. Then, C_{i1} can be simplified as (12) shown at the bottom of the next page.

After C_{i1} is determined, the self-capacitance C_{i2} and cross-coupling mutual capacitance C_{Miakb} can also be acquired with $V_{11} = V_{12} = \ldots = V_{n1} = V_{n2} = V_3 = 0$, $V_{i2} \neq 0$; $V_{11} = V_{12} = \ldots = V_{n1} = V_{n2} = V_3 = 0$ and $V_{ia} \neq 0$, respectively. The calculation equations are as follows:

$$\begin{cases} C_{i2} = \left.\frac{I_{i2}}{j\omega V_{i2}}\right|_{V_{i2} \neq 0,\quad V_3 = V_{11} = \cdots = V_{n2} = 0} \\ C_{Miakb} = \left.-\frac{I_{i1}}{j\omega V_{k2}}\right|_{V_{ia} \neq 0,\quad V_3 = V_{11} = \cdots = V_{n2} = 0} \end{cases}. \tag{13}$$

According to the symmetry of the IMCC, C_{i2} and C_{Miakb} can be simplified as shown in (14) and (15) shown at the bottom of the next page. It is worth noting the importance of (12), (14), and (15), which reveal that the computation of the equivalent circuit for a symmetrical coupler with an arbitrary number of channels and plates does not require the utilization of all coupling capacitors, thereby significantly simplifying the modeling process of the coupler.

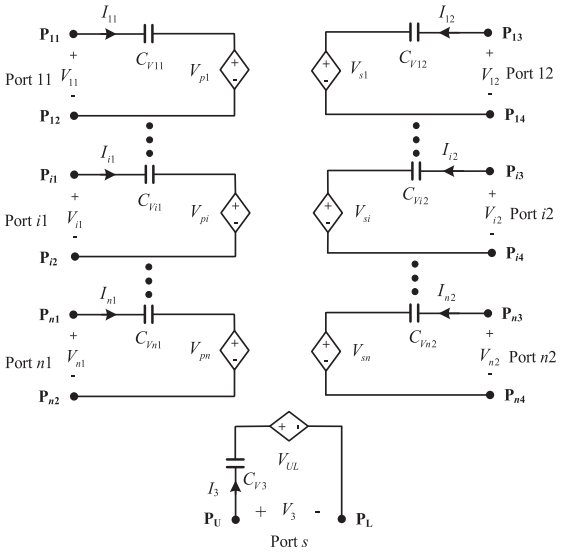

Fig. 8. IVS model of the IMCC.

D. IVS Model of the IMCC Considering Cross-Coupling

Through the ICS model, the self-capacitances and mutual capacitances of every channel, and cross-coupling mutual capacitances between different channels in the IMCC can be acquired. However, it can be seen from (12) and (14) that the self-capacitances in the ICS model are coupling dependent, which means it will change with the misalignment of the coupler. Hence, based on the ICS model, the IVS model is further used for the IMCC due to its coupling independent of self-capacitances, and the equivalent series self-capacitances are convenient for compensation parameters calculation [32].

For the IMCC, the IVS model is shown in Fig. 8. V_{i1} and V_{i2} represent the input and output voltage of channel i, and I_{i1} and I_{i2} represent the input and output current of channel i. C_{Vi1}, C_{Vi2}, and C_{VMi} represent the transmitting-side self-capacitance, the receiving-side self-capacitance, and the mutual capacitance of channel i in the IVS model. The cross-coupling mutual capacitances between port a of channel i and port b of channel k are defined as $C^{ik}{}_{Mab}$ ($a = 1,2$, $b = 1,2$). It is clear that $C^{ii}{}_{M12} = C_{VMi}$. The equivalent capacitances in the IVS model can be determined as follows based on the calculation results of the ICS model:

$$\begin{cases} C_{Vi1} = \frac{C_{i1}C_{i2} - C_{Mi1i2}C_{Mi1i2}}{C_{i2}} \\ C_{Vi2} = \frac{C_{i1}C_{i2} - C_{Mi1i2}C_{Mi1i2}}{C_{i1}} \\ C_{VMi} = \frac{C_{i1}C_{i2} - C_{Mi1i2}C_{Mi1i2}}{C_{Mi1i2}} \\ C^{ik}_{Mab} = \frac{C_{ia}C_{kb} - C_{Miakb}C_{Miakb}}{C_{Miakb}} \end{cases}. \tag{16}$$

It can be seen from (16) that, for a multichannel coupler, the IVSs of a given channel are no longer related only to the mutual capacitance between the transmitting side and receiving side in the channel. Any transmitting side and receiving side in other channels may induce voltages related to cross-coupling mutual capacitances $C^{ik}{}_{Mab}$. In addition, it is important to note that the cross-coupling mutual capacitances C_{Miakb} in the ICS model are very small, whereas $C^{ik}{}_{Mab}$ related to C_{Miakb} in the IVS model is very large, which means a very small induced voltage.

E. Comparison Between the IMCC and the FMCC

An integrated three-channel coupler is composed of plates P_{11}, P_{12}, P_{13}, and P_{14} of channel 1, P_{21}, P_{22}, P_{23}, and P_{24} of channel 2, P_{31}, P_{32}, P_{33}, and P_{34} of channel 3, and P_U and P_L. According to (12), (14), and (15), the self-capacitances and mutual capacitances of every channel, and cross-coupling mutual capacitances between different channels are calculated as shown in Table I. It can be seen from Table I that, compared to the FMCC (without P_U and P_L), the self-capacitances in the IMCC are larger due to the presence of shielding plates, whereas the mutual capacitances and cross-coupling mutual capacitances are basically equivalent.

ANSYS Maxwell is used to perform FEA of three-channel IMCC and FMCC. Set the dimensions as shown in Table II. The influence of plate thickness ($t = 2$ mm) on the couplings can be neglected. The X, Y, and Z directions are defined in Fig. 3. The calculated self-capacitances and mutual capacitances in the ICS model of channel 2 are shown in Fig. 9.

It can be seen from Fig. 9 that the primary and secondary self-capacitances are equal due to the symmetry of the coupler. In addition, either in the case of alignment or misalignment, the self-capacitances of IMCC are significantly larger than those of FMCC, whereas the mutual capacitances are basically the same. Therefore, smaller compensation inductors are needed to

$$C_{i1} = \left[C^{i}_{12} + \sum_{k=0}^{n} \frac{C^{ka}_{r1}C^{ka}_{r2}}{\left(C^{ka}_{r1} + C^{ka}_{r2} + C^{ka}_{t}\right)}\right] + \frac{\left[C^{i2}_{r2} + \sum_{k=0}^{n} \frac{C^{ka}_{r2}C^{ka}_{t}}{\left(C^{ka}_{r1}+C^{ka}_{r2}+C^{ka}_{t}\right)}\right] \times \left[C^{i2}_{r1} + \sum_{k=0}^{n} \frac{C^{ka}_{t}C^{ka}_{r1}}{\left(C^{ka}_{r1}+C^{ka}_{r2}+C^{ka}_{t}\right)}\right]}{\left[\left(C^{i2}_{r1} + C^{i2}_{r2}\right) + \sum_{k=0}^{n} \frac{C^{ka}_{t}\left(C^{ka}_{r1}+C^{ka}_{r2}\right)}{\left(C^{ka}_{r1}+C^{ka}_{r2}+C^{ka}_{t}\right)}\right]} \tag{11}$$

$$C_{i1} = C^{i}_{12} + \frac{\left(C^{i}_{13} + C^{i}_{14} + C^{is}_{1U} + C^{is}_{1L}\right)}{2} + \frac{\sum_{k=1}^{n}\left(C^{ik}_{11} + C^{ik}_{12} + C^{ik}_{13} + C^{ik}_{14}\right)}{2}. \tag{12}$$

$$C_{i2} = C^{i}_{34} + \frac{\left(C^{i}_{31} + C^{i}_{32} + C^{is}_{3U} + C^{is}_{3L}\right)}{2} + \frac{\sum_{k=1}^{n}\left(C^{ik}_{31} + C^{ik}_{32} + C^{ik}_{33} + C^{ik}_{34}\right)}{2} \tag{14}$$

$$C_{Miakb} = \frac{C^{ik}_{11} - C^{ik}_{12}}{2}, \quad a = b \qquad C_{Miakb} = \frac{C^{ik}_{13} - C^{ik}_{14}}{2}, \quad a \neq b \qquad C_{Mia0s} = 0. \tag{15}$$

TABLE I
CAPACITANCES OF A THREE-CHANNEL IMCC WHEN WELL ALIGNED

Channel #1	Channel #2	Channel #3
$C_{11}=C_{12}^{1}+\frac{C_{13}^{1}+C_{14}^{1}+C_{1U}^{1s}+C_{1L}^{1s}}{2}+\frac{C_{11}^{12}+C_{12}^{12}+C_{13}^{12}+C_{14}^{12}}{2}+\frac{C_{11}^{13}+C_{12}^{13}+C_{13}^{13}+C_{14}^{13}}{2}$	$C_{21}=C_{12}^{2}+\frac{C_{13}^{2}+C_{14}^{2}+C_{1U}^{2s}+C_{1L}^{2s}}{2}+\frac{C_{11}^{21}+C_{12}^{21}+C_{13}^{21}+C_{14}^{21}}{2}+\frac{C_{11}^{23}+C_{12}^{23}+C_{13}^{23}+C_{14}^{23}}{2}$	$C_{31}=C_{12}^{3}+\frac{C_{13}^{3}+C_{14}^{3}+C_{1U}^{3s}+C_{1L}^{3s}}{2}+\frac{C_{11}^{31}+C_{12}^{31}+C_{13}^{31}+C_{14}^{31}}{2}+\frac{C_{11}^{32}+C_{12}^{32}+C_{13}^{32}+C_{14}^{32}}{2}$
$C_{12}=C_{34}^{1}+\frac{C_{31}^{1}+C_{32}^{1}+C_{3U}^{1s}+C_{3L}^{1s}}{2}+\frac{C_{31}^{12}+C_{32}^{12}+C_{33}^{12}+C_{34}^{12}}{2}+\frac{C_{31}^{13}+C_{32}^{13}+C_{33}^{13}+C_{34}^{13}}{2}$	$C_{22}=C_{34}^{2}+\frac{C_{31}^{2}+C_{32}^{2}+C_{3U}^{2s}+C_{3L}^{2s}}{2}+\frac{C_{31}^{21}+C_{32}^{21}+C_{33}^{21}+C_{34}^{21}}{2}+\frac{C_{31}^{23}+C_{32}^{23}+C_{33}^{23}+C_{34}^{23}}{2}$	$C_{32}=C_{34}^{3}+\frac{C_{31}^{3}+C_{32}^{3}+C_{3U}^{3s}+C_{3L}^{3s}}{2}+\frac{C_{31}^{31}+C_{32}^{31}+C_{33}^{31}+C_{34}^{31}}{2}+\frac{C_{31}^{32}+C_{32}^{32}+C_{33}^{32}+C_{34}^{32}}{2}$
$C_{M1112}=\frac{C_{13}^{1}-C_{14}^{1}}{2}$	$C_{M2122}=\frac{C_{13}^{2}-C_{14}^{2}}{2}$	$C_{M3132}=\frac{C_{13}^{3}-C_{14}^{3}}{2}$
$C_{M1121}=C_{M1222}=\frac{C_{11}^{12}-C_{12}^{12}}{2}$, $C_{M1122}=C_{M1221}=\frac{C_{13}^{12}-C_{14}^{12}}{2}$	$C_{M2131}=C_{M2232}=\frac{C_{11}^{23}-C_{12}^{23}}{2}$, $C_{M2132}=C_{M2231}=\frac{C_{13}^{23}-C_{14}^{24}}{2}$	
$C_{M1131}=C_{M1232}=\frac{C_{11}^{13}-C_{12}^{13}}{2}$, $C_{M1132}=C_{M1231}=\frac{C_{13}^{13}-C_{14}^{13}}{2}$		

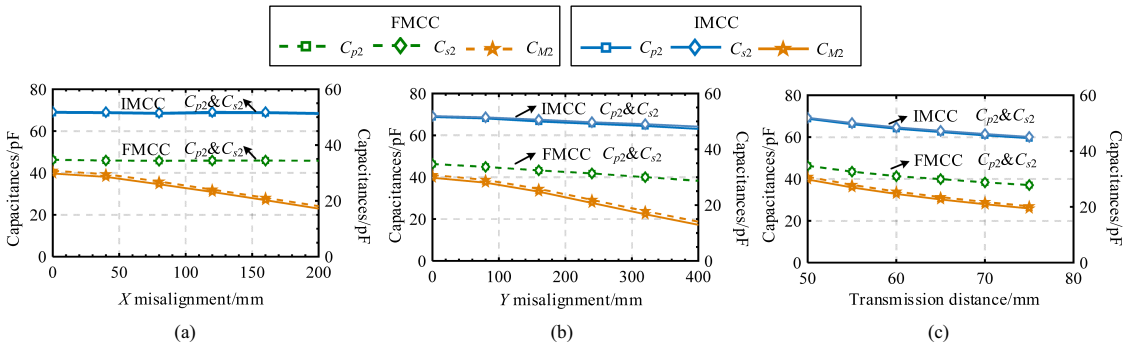

Fig. 9. Variation curves of self-capacitances and mutual capacitances for FMCC and IMCC in the ICS model. (a) X-axis misalignment. (b) Y-axis misalignment. (c) Transmission distance change.

TABLE II
SIMULATED PARAMETERS OF THREE-CHANNEL COUPLER

Parameter	Value	Parameter	Value
l_1/mm (IMCC)	1500	d_1/mm	50
l_2/mm (IMCC)	2000	d_2/mm (IMCC)	50
l_3/mm	400	d_3/mm	50
l_4/mm	800	d_4/mm	200

resonate with IMCC, and shunt capacitors are unnecessary in the CPT system. Combined with (16), larger self-capacitances and the same cross-coupling mutual capacitances also mean that the cross-coupling mutual capacitances in the IVS model of IMCC are larger than those of FMCC.

III. REDUCED CROSS-COUPLING EFFECTS OF THE IMCC ON AN M-M COMPENSATED CPT SYSTEM

A. Simplification of Cross-coupling Effects

The above analysis shows that in a multichannel coupler, cross-coupling mutual capacitances exist between any two ports of different channels. To simplify analysis, the ratio of cross-coupling mutual capacitances to the mutual capacitances is calculated by using the FEA results with Table II, as shown in Fig. 10.

Fig. 10(a) shows the ratio of cross-coupling mutual capacitances to the mutual capacitances, where r_{1121} and r_{1122} are the ratio between port 11 of channel 1 and ports 21 and 22 of channel 2, r_{1131} and r_{1132} are for port 11 of channel 1 and ports 31 and 32 of channel 3. It can be seen that as the separation distance d_3 increases, cross-coupling mutual capacitances decrease rapidly. The cross-coupling mutual capacitances between adjacent channels are much larger than discrete channels. In addition, the same-side cross-coupling mutual capacitances are larger than the different-side cross-coupling mutual capacitances.

Fig. 10(b) and (c) shows that the same-side cross-coupling mutual capacitances and different-side cross-coupling mutual capacitances ratios are also related to the transmission distance d_1, and the larger the transmission distance, the higher the ratio, which is mainly due to the rapid decrease of the mutual capacitances. However, when the separation distance between channels is greater than 100 mm (25% of the length of transmission plates), the ratio of both same-side and different-side cross-coupling mutual capacitance is below 5%.

To summarize, both the same-side and different-side cross-coupling mutual capacitances generated between adjacent channels need to be considered, whereas the cross-coupling mutual

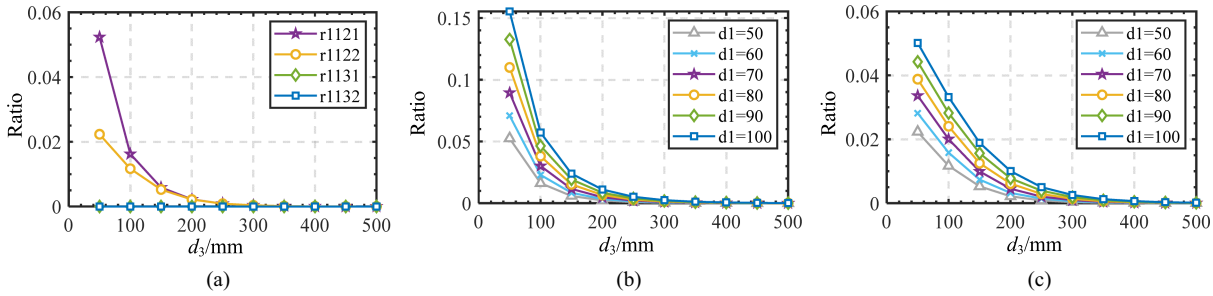

Fig. 10. Ratio of cross-coupling mutual capacitances to mutual capacitances. (a) Cross-coupling mutual capacitance ratio between channel 1 and channels 2 and 3. (b) Same-side cross-coupling mutual capacitance ratio to mutual capacitances C_{M1121}/C_{M1}. (c) Different-side cross-coupling mutual capacitances ratio to mutual capacitances C_{M1122}/C_{M1}.

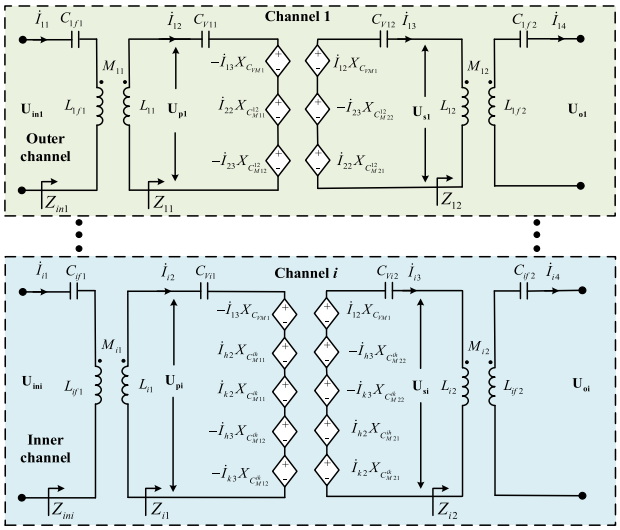

Fig. 11. Equivalent AC circuit topology of an M-M compensated multichannel CPT system considering cross-coupling.

capacitances between discrete channels are very small, which can be neglected.

B. Effects Caused by Cross-coupling Mutual Capacitances on the M-M Compensated CPT System

M-M compensation network is adopted in the multichannel CPT system. Compared to higher-order compensation networks such as LCL-LCL and CLL-CLL, it offers advantages of high design freedom, small voltage-current stresses of compensation elements, and additional isolation [12], [25], [38]. The equivalent ac circuit topology considering cross-coupling of adjacent channels is shown in Fig. 11. The channels of system can be distinguished as outer channels (green) and inner channels (blue), with the outer channels being channels 1 and n, which are affected by the cross-coupling mutual capacitances of one adjacent channel, and the other channels being the inner channels, which are affected by the cross-coupling mutual capacitances of two adjacent channels. $\boldsymbol{U_{pi}}$ and $\boldsymbol{U_{si}}$ indicate the input and output voltage of the coupler.

The resonant conditions of the system are designed as (17).

$$\begin{cases} \omega^2 L_{if1} C_{if1} = 1, & \omega^2 L_{if2} C_{if2} = 1 \\ \omega^2 L_{i1} C_{Vi1} = 1, & \omega^2 L_{i2} C_{Vi2} = 1. \end{cases} \tag{17}$$

The voltage and current equations for the outer and inner channels can be calculated as (18) shown at the bottom of this page. X represents the impedance of mutual capacitances. With equal separation distance between channels, the different-side cross-coupling mutual capacitances are equal, and the same-side cross-coupling mutual capacitances are equal too.

$$\begin{cases} C_{Maa}^{ik} = C_{M\alpha} \\ C_{Mab}^{ik} = C_{M\beta}, \quad a \neq b \end{cases}. \tag{19}$$

In addition, due to the parallel connection at the dc input side and output side, the rms value of the input voltage of different channels is equal, as well as the rms value of the output voltage.

$$\begin{cases} U_{ini} = U_{inj} \\ U_{oi} = U_{oj} \end{cases}. \tag{20}$$

According to the characteristics of the M-M compensation network under resonant conditions, the input and output currents of the coupler can be calculated as

$$\begin{cases} I_{i2} = \frac{jU_{ini}}{\omega M_{i1}} \\ I_{i3} = \frac{U_{oi}}{j\omega M_{i2}} \end{cases}. \tag{21}$$

M_{i1} and M_{i2} represent the primary and secondary mutual inductances, which can be calculated as follows:

$$M_{i1} = M_{i2} = k_{i1}\sqrt{L_{if1}L_{i1}} = k_{i2}\sqrt{L_{if2}L_{i2}} \tag{22}$$

$$\text{outer channel} \begin{cases} \dot{U}_{pi} = -\dot{I}_{i3}X_{C_{VMi}} + \dot{I}_{(i\pm1)2}X_{C_{M11}^{i(i\pm1)}} - \dot{I}_{(i\pm1)3}X_{C_{M12}^{i(i\pm1)}} \\ \dot{U}_{si} = \dot{I}_{i2}X_{C_{VMi}} - \dot{I}_{(i\pm1)3}X_{C_{M22}^{i(i\pm1)}} + \dot{I}_{(i\pm1)2}X_{C_{M21}^{i(i\pm1)}} \end{cases} \quad i = 1, n$$

$$\text{inner channel} \begin{cases} \dot{U}_{pi} = -\dot{I}_{i3}X_{C_{VMi}} + \dot{I}_{(i-1)2}X_{C_{M11}^{i(i-1)}} + \dot{I}_{(i+1)2}X_{C_{M11}^{i(i+1)}} - \dot{I}_{(i-1)3}X_{C_{M12}^{i(i-1)}} - \dot{I}_{(i+1)3}X_{C_{M12}^{i(i+1)}} \\ \dot{U}_{si} = \dot{I}_{i2}X_{C_{VMi}} - \dot{I}_{(i-1)3}X_{C_{M22}^{i(i-1)}} - \dot{I}_{(i+1)3}X_{C_{M22}^{i(i+1)}} + \dot{I}_{(i-1)2}X_{C_{M21}^{i(i-1)}} + \dot{I}_{(i+1)2}X_{C_{M21}^{i(i+1)}} \end{cases} \quad i = 2, 3, \ldots n-1. \tag{18}$$

where k_{i1} and k_{i2} are the coupling coefficients of L_{if1} and L_{i1}, L_{if2}, and L_{i2}.

Combining (20) and (21), it is clear that the input current I_{i2} of different channels is equal so as the output current I_{i3} of different channels.

$$\begin{cases} I_{12} = I_{22} = \cdots = I_{i2} = \cdots = I_{n2} = I_p \\ I_{13} = I_{23} = \cdots = I_{i3} = \cdots = I_{n3} = I_s \end{cases}. \tag{23}$$

The impedance of same-side and different-side cross-coupling mutual capacitances is defined as $X_{CM\alpha}$ and $X_{CM\beta}$. The voltage (18) can be simply expressed as follows:

$$\begin{aligned} &\text{outer channel} \begin{cases} \dot{U}_{pi} = -\dot{I}_s X_{C_{VMi}} + \dot{I}_p X_{C_{M\alpha}} - \dot{I}_s X_{C_{M\beta}} \\ \dot{U}_{si} = \dot{I}_p X_{C_{VMi}} - \dot{I}_s X_{C_{M\alpha}} + \dot{I}_p X_{C_{M\beta}} \end{cases} \\ &\text{inner channel} \begin{cases} \dot{U}_{pi} = -\dot{I}_s X_{C_{VMi}} + 2\dot{I}_p X_{C_{M\alpha}} - 2\dot{I}_s X_{C_{M\beta}} \\ \dot{U}_{si} = \dot{I}_p X_{C_{VMi}} - 2\dot{I}_s X_{C_{M\alpha}} + 2\dot{I}_p X_{C_{M\beta}} \end{cases} \end{aligned}. \tag{24}$$

Under resonant conditions, the input impedance of outer and inner channels can be calculated as follows:

$$\begin{cases} Z_{\text{in\_outer}} = (\omega M_{i1})^2 / \left[X_{C_{VM\alpha}} - \dfrac{\left(X_{C_{VMi}} + X_{C_{VM\beta}}\right)^2}{\left(X_{C_{VM\alpha}} + \frac{(\omega M_{i2})^2}{R_{eqi\_\text{outer}}}\right)} \right] \\ Z_{\text{in\_inner}} = (\omega M_{i1})^2 / \left[2X_{C_{VM\alpha}} - \dfrac{\left(X_{C_{VMi}} + 2X_{C_{VM\beta}}\right)^2}{\left(2X_{C_{VM\alpha}} + \frac{(\omega M_{i2})^2}{R_{eqi\_\text{inner}}}\right)} \right] \end{cases}. \tag{25}$$

It can be seen from (25) that the input impedance of both outer and inner channels is no longer purely resistive due to the influence of cross-coupling mutual capacitances. This means the system loses ZPA, and the output power and the efficiency will be affected. In addition, the impedance of the outer and inner channels is different, which will lead to the output unbalance between channels.

Therefore, eliminating or reducing the cross-coupling mutual capacitances in a multichannel coupler is important to maintain system output balance and high efficiency. According to (25), if the ratio of impedance $X_{CVM\alpha}$ and $X_{CVM\beta}$ to X_{CVMi} is very small, the cross-coupling effect can be nearly neglected. As such, when the ratio of C_{VMi} to $C_{VM\alpha}$ and $C_{VM\beta}$ is very small, the IVSs will be mainly related only to the mutual capacitance between the transmitting side and receiving side in the channel.

Fig. 12 shows that when the FMCC and IMCC are aligned, the ratio of mutual capacitances to cross-coupling mutual capacitances is below 0.05, which means the IVSs caused by cross-coupling mutual capacitances are much smaller than the mutual capacitances. In addition, the effects of different-side cross-coupling mutual capacitances are weaker than the same side. When FMCC and IMCC are deviated, the ratios of capacitances are both increasing. However, the ratios of capacitances for IMCC are always lower than for the FMCC. In other words, the IMCC has well capability to reduce cross-coupling effects.

C. System Parametric Design

When designing the high-power multichannel CPT system, the demands of output power are usually determined according to the application requirements. Then, the channel number is defined considering the constraint of a single inverter and rectifier capacity. In addition, the input/output voltage and the frequency are determined according to practical demands. The coupler size is designed based on installation space restrictions. For high-power output, the optimization strategy should improve the coupling coefficient k_{ci}. This means increasing the size of plates and shielding distance while decreasing the transmission distance. The capacitances between any two plates can be achieved by FEA, and the self-capacitance, mutual capacitance, and coupling coefficient can be calculated according to (12), (14), and (15). On this basis, all the parameters of compensation elements can be calculated according to the resonant conditions and the expression of output power. Finally, simulations should be conducted using LTspice to verify whether the output power is satisfied. The design flowchart of the system parameters is shown in Fig. 13.

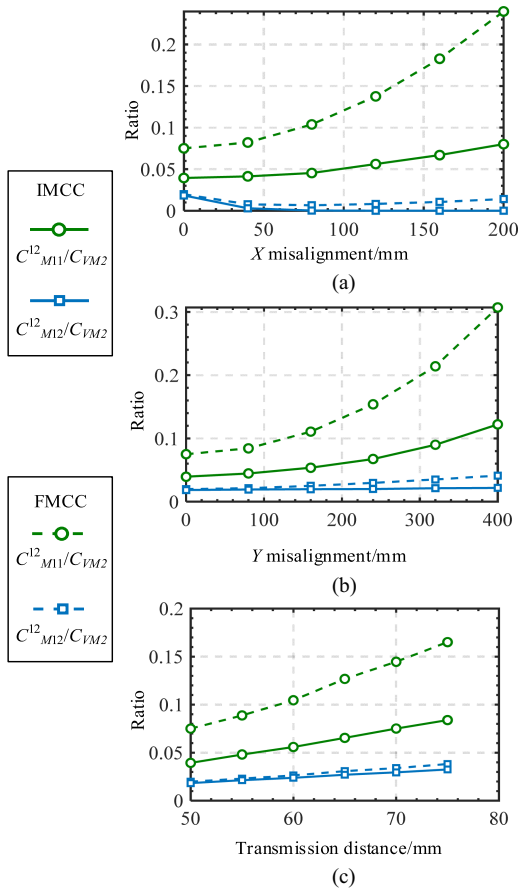

Fig. 12. Variation curves of the ratio between mutual capacitances and cross-coupling mutual capacitances for FMCC and IMCC in the IVS model. (a) *X*-axis misalignment. (b) *Y*-axis misalignment. (c) Transmission distance.

IV. Experimental Verification

A. Experimental Setup

To verify the high-power transfer capability of the multichannel CPT system and the reduced-cross-coupling characteristic of the IMCC, a 10.35-kW three-channel CPT prototype with the

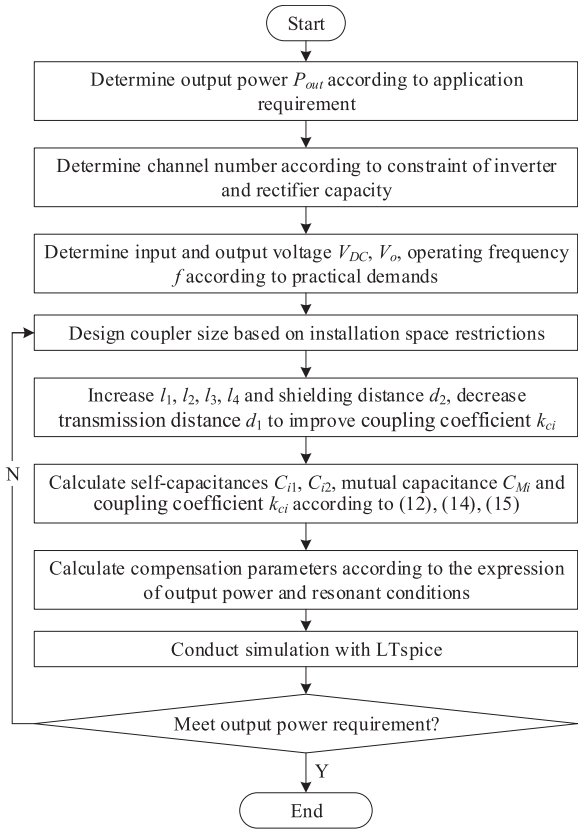

Fig. 13. Flowchart of system parametric design.

TABLE III
PARAMETERS OF THE THREE-CHANNEL CPT PROTOTYPE WITH THE IMCC

Parameter	Value	Parameter	Value
V_{DC}/V	500	V_o/V	500
C_{1f1},C_{2f1},C_{3f1}/nF	1	k_{11},k_{21},k_{31}	0.4
L_{1f1},L_{2f1},L_{3f1}/μH	26.1	k_{12},k_{22},k_{32}	0.4
C_{1f1},C_{2f2},C_{3f2}/nF	1	C_{11},C_{21},C_{31}/pF	68.0
L_{1f2},L_{2f2},L_{3f2}/μH	26.1	C_{12},C_{22},C_{32}/pF	68.0
L_{11},L_{21},L_{31}/μH	462.5	C_{M1},C_{M2},C_{M3}/pF	30
L_{12},L_{22},L_{32}/μH	462.5	f/MHz	1

IMCC is established, as shown in Fig. 14. Experimental parameters are designed according to Fig. 13, as shown in Table III. The prototype mainly consists of the dc source, inverters #1, #2, and #3, transmitting-side and receiving-side M-M compensation networks, the IMCC, uncontrolled rectifiers #1, #2, and #3, and the electronic load.

The compensation air-core inductors are wound with Litz wire to minimize high-frequency losses. L_{if1} and L_{if2} utilize 4500 strands of 0.04-mm Litz wire due to higher currents, whereas L_{i1} and L_{i2} utilize 2000 strands of 0.04-mm Litz wire. The compensation capacitors are formed by multiple film capacitors in series and parallel to achieve the required capacitance value and increase their voltage and current tolerance.

The electric field coupler IMCC is composed of fourteen aluminum plates. Four aluminum plates of size 400 × 800 × 2 mm are served as transmission plates of channels #1, #2, and #3. Two aluminum plates of size 1500 × 2000 × 2 mm

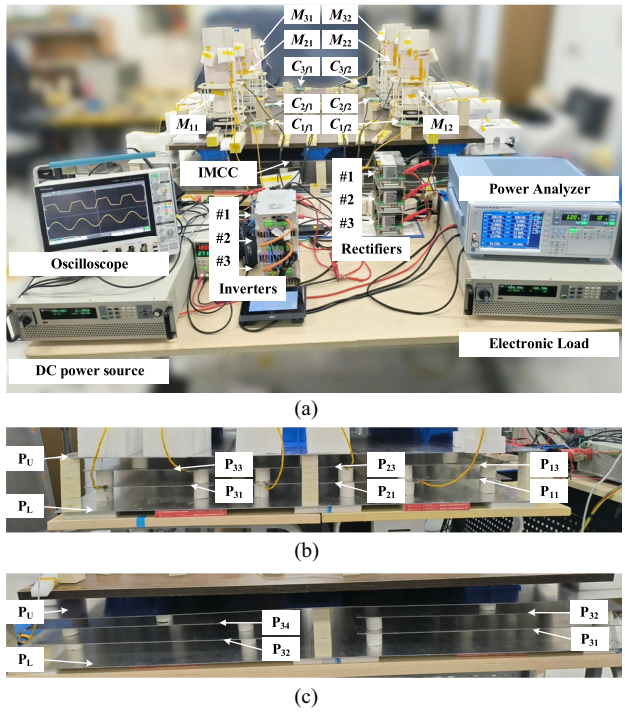

Fig. 14. Experimental platform. (a) Three-channel prototype. (b) IMCC (back view). (c) IMCC (right view).

are the shielding plates for all three channels. The transmission distance d_1 is 5 cm, and the shielding distance d_2 is 5 cm. The separated distances d_3 and d_4 are set as 10 and 20 cm to enhance cross-coupling in the context of security. To conveniently analyze the characteristics of the IMCC under varying transmission distances, shielding distances, and separation distances, the transmission and shielding plates were not encapsulated during experiments. The power analyzer WT1804E is used for efficiency and power analysis, and the oscilloscope Tektronix MSO46 is used to measure the voltage and current waveforms.

B. Verification of High-Power Transfer Performance of Proposed System

To verify the high-power transfer performance of the proposed multichannel CPT system, the output voltage and current of each inverter, the output power of each channel, the total output power, and the efficiency of the system, measured in the case of the IMCC, are well aligned and have a 5-cm offset at the X-axis.

Fig. 15(a) shows the experimental waveforms of inverter output voltages and currents for each channel under rated operating conditions. The waveforms demonstrate a well-resonant state, with $\boldsymbol{I_{in1}}$, $\boldsymbol{I_{in2}}$, and $\boldsymbol{I_{in3}}$ slightly lagging $\boldsymbol{U_{in1}}$, $\boldsymbol{U_{in2}}$, and $\boldsymbol{U_{in3}}$, respectively, which indicates the ZVS is realized. Fig. 15(b) shows the inverter output voltages and currents when the IMCC is 5-cm offset on the X-axis. It can be seen that the total output power is smaller than that of the well-aligned case, because the mutual capacitances decrease when the coupler is misaligned. In addition, it is noted that the waveforms of the inverter output voltage are not standard rectangle. The main reason for this phenomenon is the large deadtime of switch devices to avoid

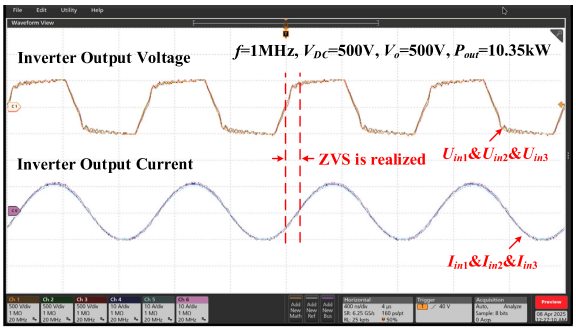

(a)

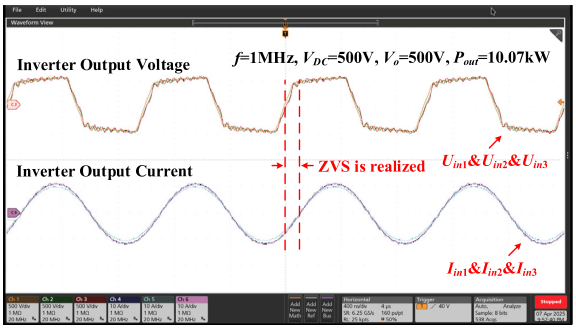

(b)

Fig. 15. Output waveforms of inverters for the M-M compensated three-channel CPT prototype with the IMCC. (a) Well aligned. (b) $\Delta X = 5$ cm.

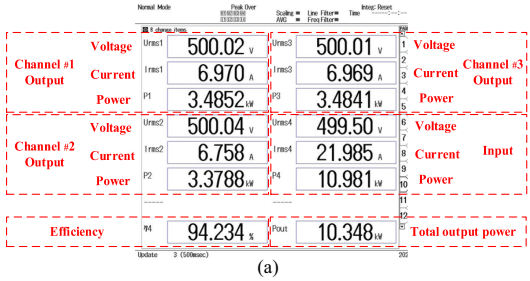

(a)

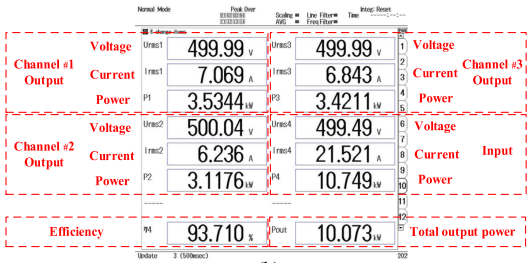

(b)

Fig. 16. Maximum efficiency for the M-M compensated three-channel CPT prototype with the IMCC. (a) Well aligned. (b) $\Delta X = 5$ cm.

short-circuiting the dc voltage source and to leave a sufficient margin for ZVS.

Fig. 16(a) shows the input power of the system and the output power of each channel when the coupler is aligned. The output power of the system reaches an impressive 10.35 kW, with a dc–dc efficiency of 94.23%. The output power of the system is three times that of each channel, demonstrating the high-power transfer performance of the proposed multichannel CPT system. Fig. 16(b) shows that when the coupler is misaligned, leading to inconsistent parameters of each channel, which in turn results

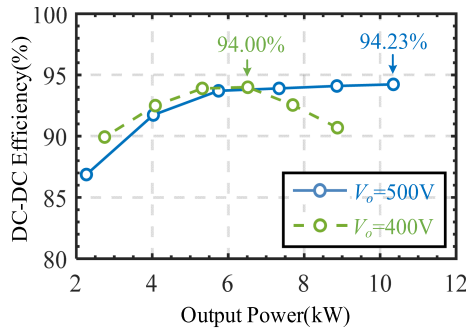

Fig. 17. Efficiency-power curves for different load conditions.

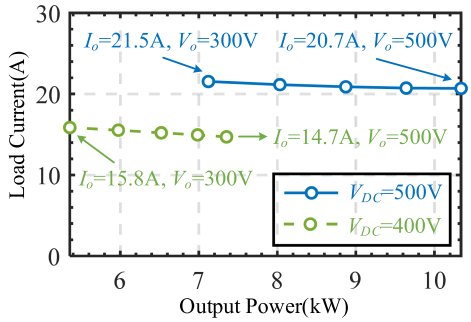

Fig. 18. Constant output current characteristics of the system.

in output imbalance between channels. The total output power and efficiency are slightly lower, but the system can still work stably.

Next, system efficiency is tested under load conditions of $V_{\mathrm{o}} = 500$ V and 400 V, as shown in Fig. 17. For each load condition, V_{DC} ranged from 250 to 500 V in 50-V increments. It can be seen that the output power increases with $\boldsymbol{U_{in}}$ and $\boldsymbol{U_o}$. The maximum power points under both load conditions occur at $V_{\mathrm{DC}} = 500$ V. The output powers reach 10.35 kW and 8.88 kW at V_o of 500 V and 400 V, respectively. However, the maximum efficiency points are not consistent with the power points. Efficiency is 94.23% when $V_{\mathrm{DC}} = V_o = 500$ V and 94.00% when $V_{\mathrm{DC}} = V_o = 400$ V, which indicates that the maximum efficiency is achieved at the condition of $V_{\mathrm{DC}} = V_o$.

In addition, the output current under different loads is measured with V_{DC} fixed at 500 and 400 V, as shown in Fig. 18. For each input condition, V_O ranged from 300 to 500 V in 50-V increments. It can be seen that as the load changes, the proposed multichannel CPT system maintains better constant current output characteristics.

C. Verification of Reducing Cross-Coupling of the IMCC

To verify the capability of reducing cross-coupling effects for the IMCC, an experiment is carried out referring to the method in [23], which is shown in Fig. 19. In Fig. 19, channel #1 is connected with inverter #1 and rectifier #1 at the work condition. While channel #2 and channel #3 are disconnected from the inverter and rectifier. The open-circuit voltage $\boldsymbol{U_{op2}}$ and $\boldsymbol{U_{os2}}$ of channel #2, and the open-circuit voltage $\boldsymbol{U_{op3}}$ and $\boldsymbol{U_{os3}}$ of channel #3 are measured. According to (16), small cross-coupling means small mutual capacitance C_{Miakb} in the

TABLE IV
COMPARISON WITH PREVIOUS HIGH-POWER CPT SYSTEMS

Reference@year	Number of channels	Compensation network	Frequency/ MHz	Power/kW	DC–DC efficiency	Coupling area/cm^2	Transfer distance/cm
[10]@2015	1	LCLC-LCLC	1	2.4	90.8%	7442	15
[26]@2018		LCL-LCL	1	1.97	91.7%	7442	15
[36]@2020		LCLC-LCLC	1	1.5	93.6%	7442	15
[37]@2023		M-M	2.5	3.55	94.2%	883	0.8
[38]@2022		M-M	1	3	95.7%	7200	10
[11]@2024		LCL-LCL	1	6.06	92.3%	5124	6
[12]@2025		M-M	1	5.13	96.5%	7200	10
[23]@2022	2	LC-LC	0.5	1.51	81.3%	6050	3
[39]@2025		LCL-S/S-LCL	0.5	1	88.5%	1800	2
This work	**3**	**M-M**	**1**	**10.35**	**94.2%**	**6400**	**5**

Bold formatting is primarily used to highlight the indicators in this paper.

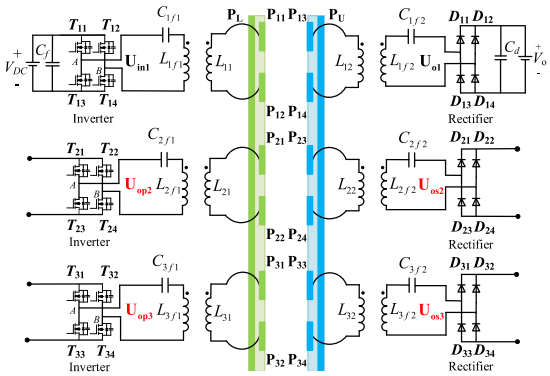

Fig. 19. Experimental verification of reducing cross-coupling of the IMCC.

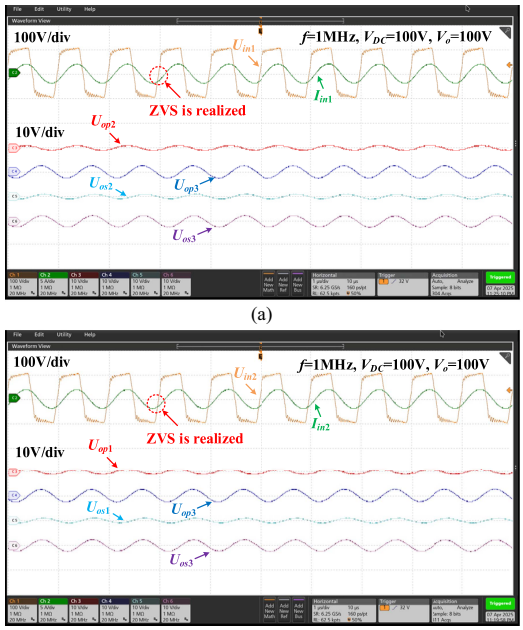

Fig. 20. Waveforms of the measuring circuit for reducing cross-coupling for the IMCC when well aligned. (a) Channel #1 is at the work condition while channel #2 and #3 are open-circuit. (b) Channel #2 is at the work condition while channel #1 and #3 are open-circuit.

ICS model and large mutual capacitance $C^{ik}{}_{Mab}$ in the IVS model, which further indicates a small induced voltage. Hence, small values of $\boldsymbol{U_{op2}}$, $\boldsymbol{U_{os2}}$,$\boldsymbol{U_{op3}}$, and $\boldsymbol{U_{os3}}$ can represent a good capability of reducing cross-coupling for the IMCC. Similarly, channel #2 is connected, whereas channel #1 and channel #2 are disconnected.

The experimental waveforms of the circuit in Fig. 19 are shown in Figs. 20 and 21. Fig. 20(a) shows the inverter output voltage and current of channel #1 and the open-circuit voltages of channel #2 and channel #3 when the IMCC is well aligned. It can be seen that when the input dc voltage of the inverter is 100 V, the maximum rms value of $\boldsymbol{U_{op2}}$, $\boldsymbol{U_{os2}}$,$\boldsymbol{U_{op3}}$, and $\boldsymbol{U_{os3}}$ is about 3 V (with 5% of the input voltage). Fig. 20(b) shows the inverter output voltage and current of channel #2 and the open-circuit voltages of channel #1 and channel #3 when IMCC is well aligned. When the input dc voltage is 100 V, the rms values of $\boldsymbol{U_{op1}}$, $\boldsymbol{U_{os1}}$,$\boldsymbol{U_{op3}}$, and $\boldsymbol{U_{os3}}$ are very small as well (about 3 V). This verifies the capability of reducing cross-coupling for the IMCC. Similar results are measured when the IMCC is 5-cm offset on the X-axis, as shown in Fig. 21, the maximum rms value of $\boldsymbol{U_{op1}}$, $\boldsymbol{U_{os1}}$,$\boldsymbol{U_{op3}}$, and $\boldsymbol{U_{os3}}$ is about 6 V.

In conclusion, the proposed IMCC has better performance of reduced cross-coupling effects when well aligned. Besides, when the IMCC is misaligned, the influence of cross-coupling increases, which is consistent with the increase in output power gap between channels. But the effect remains small due to the small cross-coupling mutual capacitances in the ICS model.

D. Discussion and Comparison

From Fig. 16(a), under rated conditions, the total system loss is calculated to be 633 W. Losses for the inverters, the rectifiers, compensation inductors, and capacitors are determined according to the models in [33], [34], and [35]. Power losses other than the above parts are assumed to be the power losses of the coupler. The loss distribution of the M-M compensated three-channel CPT prototype with the IMCC is shown in Fig. 22. It can be seen that the losses of couplers and inverters account for a larger

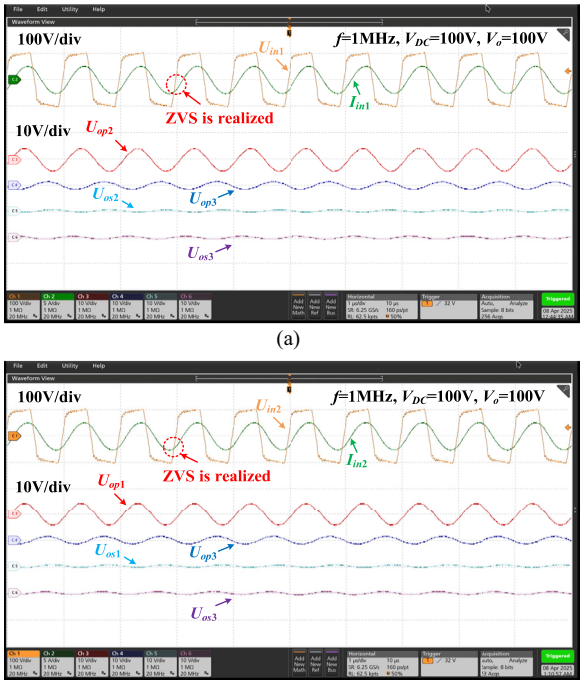

Fig. 21. Waveforms of measuring circuit for reducing cross-coupling for the IMCC when $\Delta X = 5$ cm. (a) Channel #1 is at the work condition while channel #2 and #3 are open-circuit. (b) Channel #2 is at the work condition while channel #1 and #3 are open-circuit.

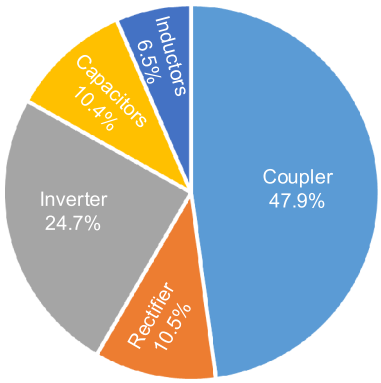

Fig. 22. Loss distribution of the M-M compensated three-channel CPT prototype with the IMCC.

portion. Future work could focus on improving the efficiency of MHz-level inverters and optimizing the design of the coupler, thereby further increasing the overall system efficiency.

Comparison with previous works of high-power CPT systems is shown in Table IV. To evaluate the implemented system, the emphasis of the comparison focuses on the output power, efficiency, and the coupler size. From the perspective of single-channel power, only [11], [12], and [37] are higher than this work, whereas the efficiency is lower in [11], the coupler size is larger in [12], and the transfer distance is too small in [37]. More importantly, this work first realizes a 10-kW-level CPT system with excellent scalability, which is meaningful for promoting CPT system applications in the field of high-power transmission.

V. Conclusion

A high-power CPT system with the IMCC is proposed in this article. The general model of the IMCC is developed with an ICS model and an IVS model. The CPT system with the IMCC is simply clarified as inner and outer channels. On this basis, the mechanism of cross-coupling effects between channels on the system is found to change the phase angle and modulus of input impedance, leading to ZPA loss, efficiency decline, and output unbalance. A comparative study of the IMCC and the FMCC reveals that the IMCC has the advantage of reducing the cross-coupling effects. A three-channel CPT system with the IMCC is built, achieving an impressive output power of 10.35 kW with 94.2% dc–dc efficiency. The experimental results demonstrate that the proposed CPT system is suitable for high-power applications, and the IMCC can effectively reduce cross-coupling capacitances. Besides, the IMCC also offers advantages of reduced compensation inductors and extendable performance.

References

[1] Y. Zhang, H. Zhou, Z. Shen, R. Xie, Z. Zheng, and X. Chen, "A family of self-adaptive interoperable receivers based on multiple decoupled receiving poles for electric vehicle wireless charging systems," *IEEE Trans. Power Electron.*, vol. 39, no. 9, pp. 11794–11802, Sep. 2024, doi: 10.1109/TPEL.2024.3404819.

[2] Y. Li et al., "Research on rectifier fault diagnosis and self-protecting for inductive power transfer system with constant-current output," *IEEE Trans. Power Electron.*, vol. 40, no. 2, pp. 3750–3769, Feb. 2025, doi: 10.1109/TPEL.2024.3484767.

[3] J. Cai, X. Wu, P. Sun, Q. Deng, J. Sun, and H. Zhou, "Design of constant-voltage and constant-current output modes of double-sided LCC inductive power transfer system for variable coupling conditions," *IEEE Trans. Power Electron.*, vol. 39, no. 1, pp. 1676–1689, Jan. 2024, doi: 10.1109/TPEL.2022.3226756.

[4] C. Chen, C. Q. Jiang, X. Wang, L. Mo, W. Guo, and S. Ren, "Terrace-shaped core design method for inductive power transfer system considering uniform magnetic flux distribution," *IEEE Trans. Ind. Electron.*, vol. 72, no. 8, pp. 7795–7806, Aug. 2025, doi: 10.1109/TIE.2025.3528499.

[5] P. Sun et al., "Eddy current loss analysis and frequency optimization design of double-sided LCC-IPT system in seawater environment," *Sci. China Technol. Sci.*, vol. 65, pp. 407–418, 2021, doi: 10.1007/s11431-021-1917-1.

[6] Z. Liu et al., "A large-area free-positioning SCC-WPT system for movable receivers," *IEEE Trans. Power Electron.*, vol. 40, no. 7, pp. 8911–8916, Jul. 2025, doi: 10.1109/TPEL.2025.3543069.

[7] X. Liu, C. Cai, S. Wu, C. Li, Q. Cui, and X. Ren, "Modeling and analysis of undersea capacitive power transfer based on conduction current in seawater," *IEEE Trans. Power Electron.*, vol. 40, no. 3, pp. 4640–4651, Mar. 2025, doi: 10.1109/TPEL.2024.3498063.

[8] C. Liang et al., "A multicell SCC capacitive coupler with strong lateral, longitudinal, and rotational antioffset performance," *IEEE Trans. Power Electron.*, vol. 40, no. 4, pp. 6230–6247, Apr. 2025, doi: 10.1109/TPEL.2024.3508769.

[9] G. Yang, P. Sun, E. Rong, X. Zhang, X. Wu, and Q. Deng, "Universal design method of load-independent constant voltage and constant current outputs for capacitive power transfer system," *IET Power Electron.*, vol. 18, no. 1, Jan. 2025, Art. no. e70016, doi: 10.1049/pel2.70016.

[10] F. Lu, H. Zhang, H. Hofmann, and C. Mi, "A double-sided LCLC-compensated capacitive power transfer system for electric vehicle charging," *IEEE Trans. Power Electron.*, vol. 30, no. 11, pp. 6011–6014, Nov. 2015, doi: 10.1109/TPEL.2015.2446891.

[11] S. Kodeeswaran, M. N. Gayathri, A. Kannabhiran, and S. S. Williamson, "Design of a static capacitive power transfer system with six-plate coupler for electric vehicle wireless charging," *IEEE Trans. Transp. Electrific.*, vol. 10, no. 2, pp. 3927–3939, Jun. 2024, doi: 10.1109/TTE.2023.3316710.

[12] E. Rong, P. Sun, G. Yang, J. Xia, Z. Liu, and S. Li, "5-kW, 96.5% efficiency capacitive power transfer system with a five-plate coupler: Design and optimization," *IEEE Trans. Power Electron.*, vol. 40, no. 1, pp. 2542–2555, Jan. 2025, doi: 10.1109/TPEL.2024.3462410.
[13] R. Bosshard and J. W. Kolar, "Multi-objective optimization of 50 kW/85 kHz IPT system for public transport," *IEEE J. Emerg. Sel. Topics Power Electron.*, vol. 4, no. 4, pp. 1370–1382, Dec. 2016, doi: 10.1109/JESTPE.2016.2598755.
[14] Q. Deng et al., "Modeling and control of inductive power transfer system supplied by multiphase phase-controlled inverter," *IEEE Trans. Power Electron.*, vol. 34, no. 9, pp. 9303–9315, Sep. 2019, doi: 10.1109/TPEL.2018.2886846.
[15] R. Liu, R. Xie, X. Chen, X. Mao, Z. Li, and Y. Zhang, "Current sharing for a multiphase inverter based on coupled external parallel resonant branches for wireless power transfer system," *IEEE Trans. Power Electron.*, vol. 40, no. 1, pp. 71–75, Jan. 2025, doi: 10.1109/TPEL.2024. 3456242.
[16] Y. Li, R. Mai, L. Lu, and Z. He, "Active and reactive currents decomposition-based control of angle and magnitude of current for a parallel multiinverter IPT system," *IEEE Trans. Power Electron.*, vol. 32, no. 2, pp. 1602–1614, Feb. 2017, doi: 10.1109/TPEL.2016.2550622.
[17] X. Liu et al., "A multi-inverter multi-rectifier wireless power transfer system for charging stations with power loss optimized control," *IEEE Trans. Power Electron.*, vol. 38, no. 8, pp. 9261–9277, Aug. 2023, doi: 10.1109/TPEL.2023.3275284.
[18] Q. Deng, P. Sun, W. Hu, D. Czarkowski, M. K. Kazimierczuk, and H. Zhou, "Modular parallel multi-inverter system for high-power inductive power transfer," *IEEE Trans. Power Electron.*, vol. 34, no. 10, pp. 9422–9434, Oct. 2019, doi: 10.1109/TPEL.2019.2891064.
[19] Y. Li, R. Mai, L. Lu, T. Lin, Y. Liu, and Z. He, "Analysis and transmitter currents decomposition based control for multiple overlapped transmitters based WPT systems considering cross couplings," *IEEE Trans. Power Electron.*, vol. 33, no. 2, pp. 1829–1842, Feb. 2018, doi: 10.1109/TPEL.2017.2690061.
[20] Y. Li et al., "Efficiency analysis and optimization control for input-parallel output-series wireless power transfer systems," *IEEE Trans. Power Electron.*, vol. 35, no. 1, pp. 1074–1085, Jan. 2020, doi: 10.1109/TPEL.2019.2914299.
[21] H. Tang et al., "A self-adaptive dual-channel LCC-S detuned topology for misalignment tolerance in AUV wireless power transfer systems," *IEEE Trans. Power Electron.*, vol. 40, no. 3, pp. 4630–4639, Mar. 2025, doi: 10.1109/TPEL.2024.3492194.
[22] Y. Liang et al., "Input-series output-series multichannel IPT system for high-voltage and high-power wireless power transfer," *IEEE J. Emerg. Sel. Topics Power Electron.*, vol. 11, no. 5, pp. 5509–5523, Oct. 2023, doi: 10.1109/JESTPE.2023.3300873.
[23] W. Zhou, Q. Gao, R. Mai, Z. He, and A. P. Hu, "Design and analysis of a CPT system with extendable pairs of electric field couplers," *IEEE Trans. Power Electron.*, vol. 37, no. 6, pp. 7443–7455, Jun. 2022, doi: 10.1109/TPEL.2021.3134708.
[24] J. Lian, X. Qu, X. Chen, and C. C. Mi, "Design of a double-sided LCLC-compensated capacitive power transfer system with predesigned coupler plate voltage stresses," *IEEE J. Emerg. Sel. Topics Power Electron.*, vol. 10, no. 1, pp. 128–137, Feb. 2022, doi: 10.1109/JESTPE.2020.3030657.
[25] E. Rong, P. Sun, K. Qiao, X. Zhang, G. Yang, and X. Wu, "Six-plate and hybrid-dielectric capacitive coupler for underwater wireless power transfer," *IEEE Trans. Power Electron.*, vol. 39, no. 2, pp. 2867–2881, Feb. 2024, doi: 10.1109/TPEL.2023.3334888.
[26] H. Zhang, F. Lu, H. Hofmann, W. Liu, and C. C. Mi, "Six-plate capacitive coupler to reduce electric field emission in large air-gap capacitive power transfer," *IEEE Trans. Power Electron.*, vol. 33, no. 1, pp. 665–675, Jan. 2018, doi: 10.1109/TPEL.2017.2662583.
[27] H. Pang, K. T. Chau, Z. Hua, and T. Yang, "Analysis of cross-coupling effect for multi-objective wireless power transfer," *IEEE Trans. Magn.*, vol. 59, no. 11, Nov. 2023, Art. no. 8401905, doi: 10.1109/TMAG.2023.3295900.
[28] Z. Zhang, H. Pang, S. H. K. Eder, and R. Kennel, "Self-balancing virtual impedance for multiple-pickup wireless power transfer," *IEEE Trans. Power Electron.*, vol. 36, no. 1, pp. 958–967, Jan. 2021, doi: 10.1109/TPEL.2020.3000045.
[29] Y. Liang et al., "Analysis and parameter design for input-series output-series (ISOS) multichannel inductive power transfer system considering cross coupling," *IEEE J. Emerg. Sel. Topics Power Electron.*, vol. 12, no. 2, pp. 2361–2376, Apr. 2024, doi: 10.1109/JESTPE.2024.3349610.
[30] W. Zhou, L. Huang, B. Luo, R. Mai, Z. He, and A. P. Hu, "A general mutual coupling model of MIMO capacitive coupling interface with arbitrary number of ports," *IEEE Trans. Power Electron.*, vol. 36, no. 6, pp. 6163–6167, Jun. 2021, doi: 10.1109/TPEL.2020.3034372.
[31] B. Regensburger, S. Sinha, A. Kumar, S. Maji, and K. K. Afridi, "High-performance multi-MHz capacitive wireless power transfer system for EV charging utilizing interleaved-foil coupled inductors," *IEEE J. Emerg. Sel. Topics Power Electron.*, vol. 10, no. 1, pp. 35–51, Feb. 2022, doi: 10.1109/JESTPE.2020.3030757.
[32] S. Wang, J. Liang, and M. Fu, "Analysis and design of capacitive power transfer systems based on induced voltage source model," *IEEE Trans. Power Electron.*, vol. 35, no. 10, pp. 10532–10541, Oct. 2020, doi: 10.1109/TPEL.2020.2981675.
[33] H. Zhang, F. Lu, H. Hofmann, W. Liu, and C. C. Mi, "A four-plate compact capacitive coupler design and LCL-compensated topology for capacitive power transfer in electric vehicle charging application," *IEEE Trans. Power Electron.*, vol. 31, no. 12, pp. 8541–8551, Dec. 2016.
[34] F. Lu, H. Zhang, H. Hofmann, and C. Mi, "A high efficiency 3.3 kW loosely-coupled wireless power transfer system without magnetic material," in *Proc. IEEE Energy Convers. Congr. Expo.*, 2015, pp. 2282–2286.
[35] Y. Li, J. Hu, F. Chen, Z. Li, Z. He, and R. Mai, "Dual-phase-shift control scheme with current-stress and efficiency optimization for wireless power transfer systems," *IEEE Trans. Circuits Syst. I, Reg. Papers*, vol. 65, no. 9, pp. 3110–3121, Sep. 2018.
[36] L. Li, Z. Wang, F. Gao, S. Wang, and J. Deng, "A family of compensation topologies for capacitive power transfer converters for wireless electric vehicle charger," *Appl. Energy*, vol. 260, Feb. 2020, Art. no. 114156, doi: 10.1016/j.apenergy.2019.114156.
[37] Y. Wang, H. Zhang, and F. Lu, "3.5-kW 94.2% dc–dc efficiency capacitive power transfer with zero reactive power circulating," *IEEE Trans. Power Electron.*, vol. 38, no. 2, pp. 1479–1484, Feb. 2023, doi: 10.1109/TPEL.2022.3215283.
[38] J. Xia, X. Yuan, S. Lu, J. Li, S. Luo, and S. Li, "A two-stage parameter optimization method for capacitive power transfer systems," *IEEE Trans. Power Electron.*, vol. 37, no. 1, pp. 1102–1117, Jan. 2022, doi: 10.1109/TPEL.2021.3097344.
[39] M. Li, J. Zheng, Y. Wang, T. Wang, F. Du, and W. Zhou, "Research on anti-misalignment characteristics of capacitive power transfer systems based on hybrid topology," in *Proc. 10th Asia Conf. Power Elect. Eng.*, 2025, pp. 863–869, doi: 10.1109/ACPEE64358.2025.11040451.

Gang Yang received the B.S. and M.S. degrees in electrical engineering, in 2014 and 2021, respectively, from the Naval University of Engineering (NUE), Wuhan, China, where he is currently working toward the Ph.D. degree in electrical engineering.

In 2019, he joined the School of Electrical Engineering, NUE, as a Lecturer. His research interests include capacitive wireless power transfer and the testability of electrical equipment.

Pan Sun received the B.S., M.S., and Ph.D. degrees in electrical engineering from te Naval University of Engineering (NUE), Wuhan, China, in 2009, 2015, and 2022, respectively.

In 2015, he joined the School of Electrical Engineering, NUE, as an Associate Professor. He has authored more than 70 papers with more than 30 being published in SCI and EI journals, such as IEEE transactions and other prestigious publications. He successively led the National Key Research and Development Program, the National Natural Science Foundation, and other research projects. His research interests include wireless power transfer, and special motors and their control.

Dr. Sun was the recipient of five provincial and ministerial awards for scientific and technological progress and teaching achievement awards.

Enguo Rong (Member, IEEE) received the B.S. degree in electrical engineering and the M.S. degree in power electronics from the Kunming University of Science and Technology (KUST), Kunming, China, in 2016 and 2019, respectively, and the Ph.D. degree in electrical engineering with the Naval University of Engineering, Wuhan, China, in 2024.

Since 2025, he has been with the Faculty of Electric Power Engineering, KUST, as a Special-Term Associate Professor. From 2019 to 2021, he was the CEO of Kunming Minya Technology Company Ltd., a company focused on the development of high-power converters. His research interests include high-frequency dc–dc converters and wireless power transfer systems.

Dr. Rong was the recipient of the Grand Prize Award from IEEE International Future Energy Challenge (IFEC) in 2017.

Xiaochen Zhang was born in Qingdao, China, in 1996. He received the B.E. degree in electrical engineering and automation from the Shanghai University of Electric Power, Shanghai, China, in 2019, and the M.E. degree in electrical engineering in 2022 from the Naval University of Engineering, Wuhan, China, where he is currently working toward the Ph.D. degree in electrical engineering.

His current research interests include capacitive power transfer technology and its applications.

Xusheng Wu received the B.Sc., M.Sc.Tech., and Ph.D. degrees from the College of Electrical and Informational Engineering, Naval University of Engineering, Wuhan, China, in 1996, 1999, and 2004, respectively.

He is currently a Professor with the College of Electrical Engineering, Naval University of Engineering. Meanwhile, he is the Vice Principal of the Naval University of Engineering and the Director of the Military Port and Island Power Engineering Military Logistics Research Laboratory. His research interests include wireless power transfer, electric devices, and power systems on warships.

Qijun Deng received the B.S. and M.Sc. degrees in mechanical engineering from Wuhan University, Wuhan, China, in 1999 and 2002, respectively, and the Ph.D. degree in computer application technology from Wuhan University, Wuhan, China, in 2005.

In 2005, he joined the Department of Automation (which now is merged into School of Electrical Engineering and Automation), Wuhan University, where he is currently a Professor. From 2013 to 2014, he was a Visiting Scholar with New York University Tandon School of Engineering, Brooklyn, NY, USA.

Siqi Li (Senior Member, IEEE) received the B.S. and Ph.D. degrees in electrical engineering from Tsinghua University, Beijing, China, in 2004 and 2010, respectively.

From 2011 to 2013, he was a Postdoctoral Fellow with the University of Michigan, Dearborn, MI, USA. From 2018 to 2019, he was a Visiting Scholar with San Diego State University, San Diego, CA, USA. In 2013, he joined the Faculty of Electric Power Engineering, Kunming University of Science and Technology (KUST), Kunming, China, where he is currently a Professor with the Department of Electrical Engineering. He is also the Director of the Advanced Power Electronics and New Energy Laboratory, KUST. His research interests include battery management systems, high-performance wired and wireless battery chargers for electric vehicles, and solid-state transformers.